The Dark Region Artifact in Adaptive Ultrasound Beamforming

Ole Marius Hoel Rindal*, Alfonso Rodriguez-Molares†, and Andreas Austeng*

*Department of Informatics
University of Oslo
Oslo, Norway
Email: omrindal@ifi.uio.no

†Department of Circulation and Medical Imaging
Norwegian University of Science and Technology
Trondheim, Norway

Abstract—An undesired effect, the *dark region artifact* (DRA), has been under-communicated in our research community. The DRA appear next to acoustically strong targets for some of the many adaptive beamformers introduced in the literature. This study investigates the DRA for a collection of adaptive beamformers and shows that this effect originates because some of the methods fail to estimate which signals arise in the mainlobe and which originates from sidelobes. The DRA results in darker regions in the ultrasound images, indicating the wrong acoustical amplitude. Therefore, the measured contrast can falsely appear higher for adaptive beamformers affected by the DRA.

Keywords—Contrast, Adaptive Beamforming, Minimum Variance Beamforming, Coherence Based Beamforming

I. Introduction

The shift to software beamforming has inspired a myriad of adaptive beamformers. Some of these misinterpret which signals originate from sidelobes and which originate from the mainlobe. This results in a dark region artifact (DRA) next to hyperechoic targets. We investigate this artifact for seven beamformers: Delay-And-Sum (DAS), the Coherence Factor (CF), Generalized Coherence Factor (GCF), Phase Coherence Factor (PCF), Delay-Multiply-And-Sum (DMAS), Capon's Minimum Variance (MV) and Eigenspace Based Minimum Variance (EBMV). We study how the DRA can invalidate the estimation of the contrast ratio (CR).

II. Background

For the sake of conciseness only the methods DMAS, GCF and EBMV are described here. The methods DAS, MV, PCF and CF are described in [1], or view the references [2] for MV, [3] and [4] for CF and [5] for PCF.

A. Delay Multiply And Sum (DMAS)

The DMAS introduced in [6] multiply the delayed RF signals using a "signed" square root;

$$\hat{y}_{ij}[z,x] = \text{sign}\left(y_i[z,x]y_j[z,x]\right)\sqrt{|y_i[z,x]y_j[z,x]|}. \quad (1)$$

where $y_i[z,x]$ is the delayed signal received for image pixel $[z,x]$ from element i, before the multiplied signals are summed over the M elements;

$$S^*_{\text{DMAS}}[z,x] = \sum_{i=1}^{M-1}\sum_{j=i+1}^{M}\hat{y}_{ij}[z,x]. \quad (2)$$

The DMAS output will have both a DC and an "artificial second harmonic" component. Therefore, the final step is to band-pass filter the S^*_{DMAS} around $2f_c$ to attenuate the DC and higher frequency components. Conventional envelope detection and log-compression follow.

B. Generalized Coherence Factor (GCF)

The CF was extended into the GCF in [4]. The GCF is defined as

$$\text{GCF}[z,x] = \frac{\text{energy in a low-frequency region}}{\text{total energy}} \quad (3)$$

$$= \frac{\sum_{k\in\text{low-frequency region}}|p[z,x,k]|^2}{\sum_{k=0}^{M-1}|p[z,x,k]|^2} \quad (4)$$

Here p is the M-point Fourier-spectrum over the aperture of the delayed channel data, where $k = 0$ to $M-1$ is the spatial frequency index. The low-frequency region is specified by a cutoff frequency M_0 in the spatial frequency index (i.e. from $-M_0$ to M_0).

The GCF is used as a weighting to the DAS image, so that

$$S_{\text{GCF}} = S_{\text{DAS}}[z,x]\text{GCF}. \quad (5)$$

We have, as the authors in [4] suggested, implemented the GCF with the fast Fourier-transform. We use $M_0 = 5$. Notice that if $M_0 = 0$ the GCF simplifies to the CF.

C. Eigenspace Based Minimum Variance Beamforming (EBMV)

The MV beamformer has been extended into the EBMV beamformer in [7]. The authors argue that by utilizing the eigenstructure of the covariance matrix they enhance the performance of the MV beamformer and improve image quality in terms of resolution and sidelobes by suppressing off-axis signals while keeping on-axis ones. The covariance matrix is estimated as described in [1] and [2]. Then, the authors propose to eigendecompose the covariance matrix;

$$\hat{\boldsymbol{R}}_{\text{DL}} = V\Lambda^{-1}V^H, \quad (6)$$

where $\Lambda = [\lambda_1, \lambda_2, ..., \lambda_L]^T$ are the eigenvalues in descending order, and $V = [v_1, v_2, ...v_L]$ are the corresponding eigenvectors. The signal subspace $\boldsymbol{E}_s$ can be constructed using the eigenvectors corresponding to the largest eigenvalues,

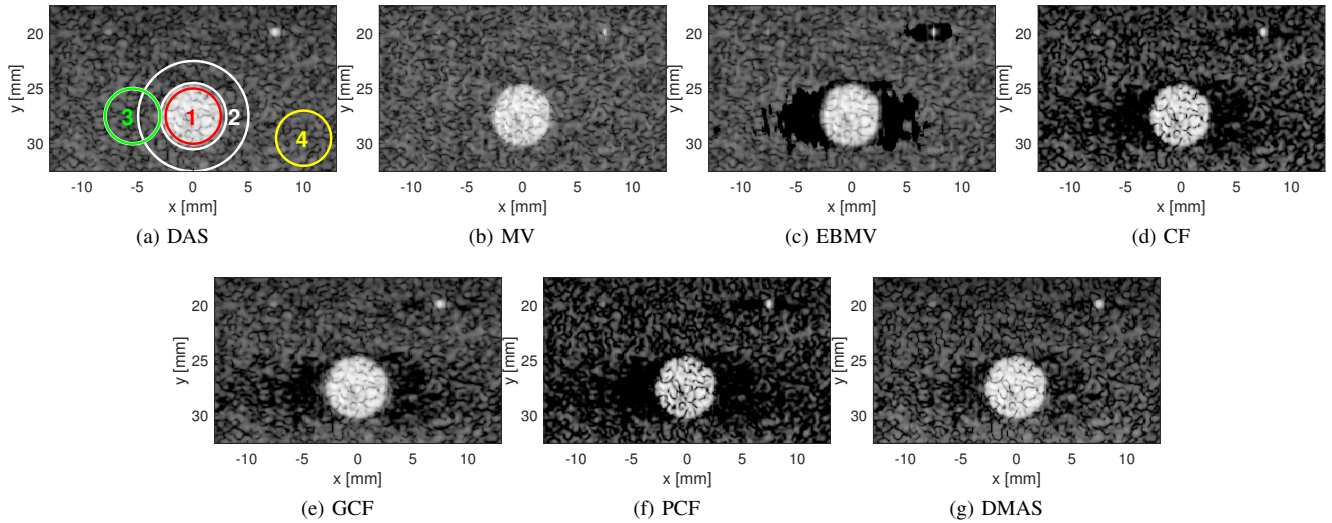$$\boldsymbol{E}_s = [v_1, ..., v_E], \quad (7)$$

Fig. 1. Simulated images for all beamformers. The images are shown with a 60 dB dynamic range. The DRA is observed for the EBMV, CF, GCF, PCF and DMAS methods on both sides of the hyperechoic cyst and of the point scatterer to the right in Fig. c-g. The DRA is not observed for DAS in (Fig. a) and MV (Fig. b).

where E is the number of eigenvectors creating the signal subspace. Finally, the EBMV weight vector is created by projecting the conventional MV weights (see [1] and [2]) onto the constructed signal subspace

$$\boldsymbol{w}_{\text{EBMV}} = \boldsymbol{E}_s \boldsymbol{E}_s^H \boldsymbol{w}_{\text{MV}}. \tag{8}$$

To decide the number of eigenvectors the authors of [7] suggest to do an adaptive selection by using the eigenvectors whose related eigenvalues are larger than δ times the largest eigenvector λ_{max}. We are using $\delta = 0.5$.

III. METHODS

The DRA is studied in both a simulated and experimental scenario. A synthetic transmit aperture imaging (STAI) dataset was simulated in Field II containing a hyperechoic cyst and two point scatterers. The hyperechoic cyst had 30 dB stronger amplitude than the background speckle, while the point targets were 30 dB and 10 dB stronger than the background speckle.

An experimental focused imaging (FI) dataset was recorded from a CIRS phantom using a Verasonics Vantage 256 scanner (Verasonics, USA). In both datasets, a L7-4 linear probe transmitting at 5 MHz was used. For the experimental FI dataset, it was recorded 128 scan lines using 32 active transducers on transmit when possible, and receiving on all 128 elements. We use boxcar apodization with a constant F-number of 1.7 on both transmit and receive for STAI, and on receive for the FI dataset.

The contrast is measured using the contrast ratio (CR) defined as

$$\text{CR} = |\mu_{\text{ROI}} - \mu_{\text{B}}|,$$

where μ_{ROI} is the mean intensity value in dB from the region of interest and μ_{B} is the mean intensity value in dB of the background region. The CR was measured between the cyst (region 1 in Fig. a) and three different regions for the background; region 2, region 3 and region 4.

All processing has been done in MATLAB (Mathworks, Natick, MA) using the UltraSound ToolBox (USTB) [8]. For the STAI dataset, we first sum each transmit sequence and

use the adaptive beamforming algorithms on the combined received aperture. All MATLAB code and datasets to process all figures and results shown in this study are available at http://www.UltraSoundToolBox.com.
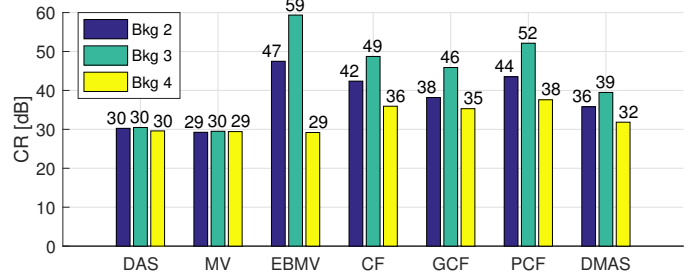

Fig. 2. Measured contrast ratio (CR) for the simulated dataset shown in Fig. 1. The CR was measured between the cyst, region 1 in Fig. 1a, and background region 2, 3 and 4.

IV. RESULTS

Fig. 1 a-g show the resulting simulated images. The DRA is observed for the EBMV, CF, GCF, PCF and DMAS methods on both sides of the hyperechoic cyst and of the point scatterer to the right in Fig. 1 c-g. The DRA is not observed for DAS in (Fig. 1a) and MV (Fig. 1b).

Fig. 2 displays the measured CR of the simulated images. We can observe that there is a large difference in the CR dependent on which background region is used. There are also variations in the CR depending on which beamforming method has been used.

The resulting experimental images are shown in Fig. 3 a-g, where the DRA is observed for the same beamforming methods as for the simulated images. The DRA is especially visible to the left and right of the point scatterer, but also on the sides of the hyperechoic cyst. The measured CR for the experimental images is displayed in Fig. 4 with the same observed variations between background regions and between the beamforming methods.
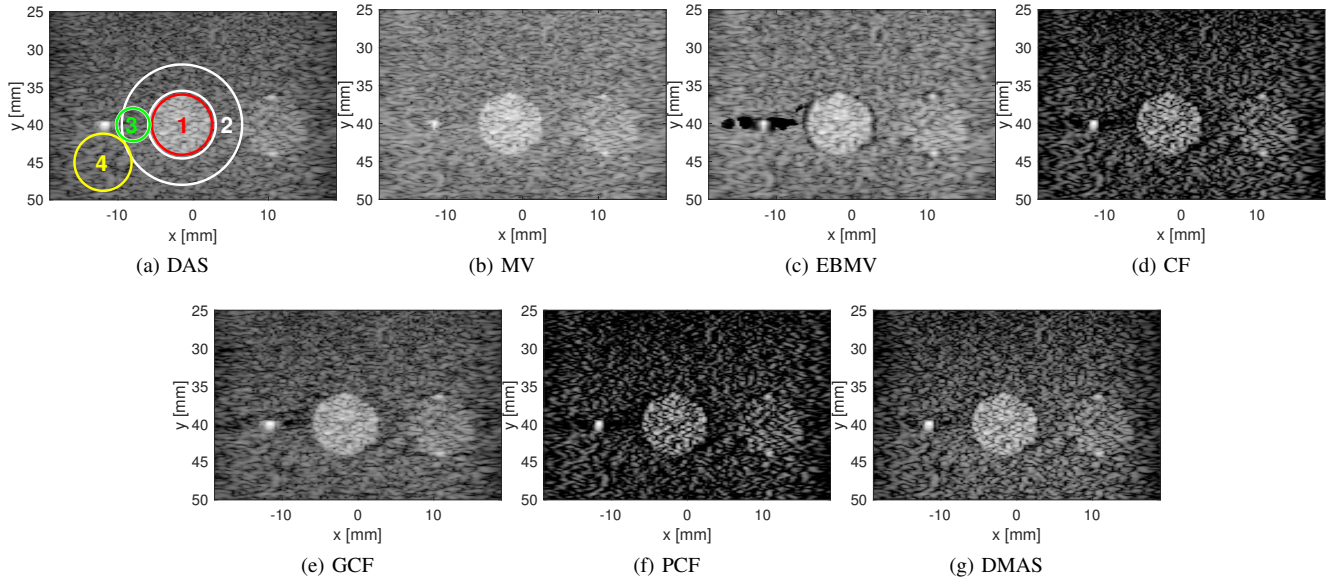
Fig. 3. Experimental images for all beamformers. The images are shown with a 60 dB dynamic range. The DRA is observed for the EBMV, CF, GCF, PCF and DMAS methods on both sides of the point scatterer and somewhat visible to the left and right of the cyst Fig. c-g. The DRA is not observed for DAS in (Fig. a) and MV (Fig. b).
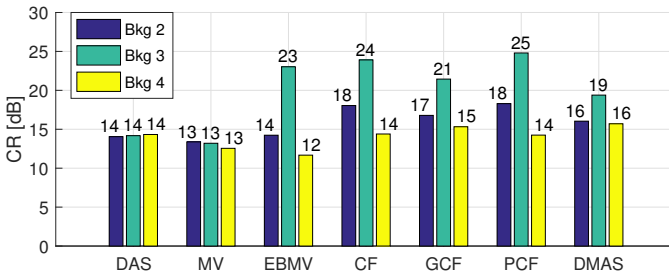

Fig. 4. Measured contrast ratio (CR) for the experimental dataset shown in Fig. 3. The CR was measured between the cyst, region 1 in Fig. 3a, and background region 2, 3 and 4.

V. DISCUSSION

The CF, GCF, PCF and DMAS methods are all using the *coherence* of the signals across the aperture in the beamforming of the images. Next to a bright structure the signals originating from the sidelobes will dominate in amplitude compared to the signals in the mainlobe. The signals in the sidelobes are off axis. Thus, the delayed wave-fronts will not align with the receiving aperture. This is illustrated in Fig. 5, where we in the top part have plotted the delayed wave-field when reconstructing the pixel exactly in the center of the point scatterer at $x = 7.5$ mm and $z = 20$ mm in Fig. 1. We are plotting the active receive channels when using expanding aperture apodization with a constant F-number of 1.7. The red line indicates which signals will contribute in the sum of "delay-and-sum" beamforming when estimating the amplitude in the pixel. Since the signals for the point scatterer is within the mainlobe, we have a correctly delayed wave-field parallel to the receiving aperture. In the middle plot we have plotted the delayed wave-field when reconstructing the pixel at $x = 7$ mm and $z = 20$ mm to the left of the point scatterer. We can observe that along the red line the wave-field is fluctuating. This is because the signal from the strong point scatterer received in the the sidelobe is stronger than the signal received by the mainlobe. Therefore, the coherence across the aperture will be low, and the beamformers utilizing coherence in the beamforming will have the DRA visible to the left of the point scatterer in Fig. 1. In the lower plot in Fig. 5 we have

plotted the delayed wave-field when reconstructing a pixel in speckle at $x = 0.0$ mm and $z = 20$ mm. We see that there are some fluctuations in the wave-field resulting in the fluctuations in the speckle pattern. However, the wave-fronts in the delayed wave-field are parallel to the receiving aperture, thus resulting in high coherence and no DRA.
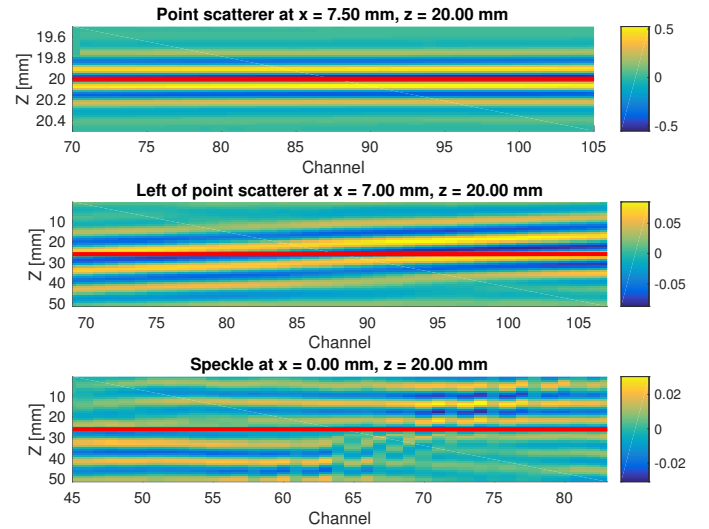

Fig. 5. The delayed wave-field for three different pixels in Fig. 1. The top is from the point scatterer at $x = 7.5$ mm and $z = 20$ mm, the middle to the left of the point scatterer at $x = 7$ mm and $z = 20$ and the bottom from the speckle pattern at $x = 0.0$ mm and $z = 20$ mm. The red line in the plot indicates the signals contributing in the sum of "delay-and-sum" beamforming when estimating the amplitude in the pixel.

The same arguments hold for the wave-fields plotted in Fig. 6. In the top plot have plotted the wave-field when reconstructing a pixel at $x = 0.0$ mm and $z = 27.5$ mm inside the hyperechoic cyst, the middle plot is the wave-field when reconstructing the pixel at $x = -4.5$ mm and $z = 27.5$ mm inside the DRA to the left of the hyperechoic cyst, and the lower plot is the wave-field when reconstructing the pixel in speckle at $x = -12.5$ mm and $z = 27.5$ mm. We see that the wave-fronts are parallel to the receive aperture for the top and

bottom wave-field. However, in the middle wave-field, once again, the strong signal from the hyperechoic cyst received in the sidelobe dominates and results in wave-fronts non-parallel to the receiving aperture resulting in the DRA.
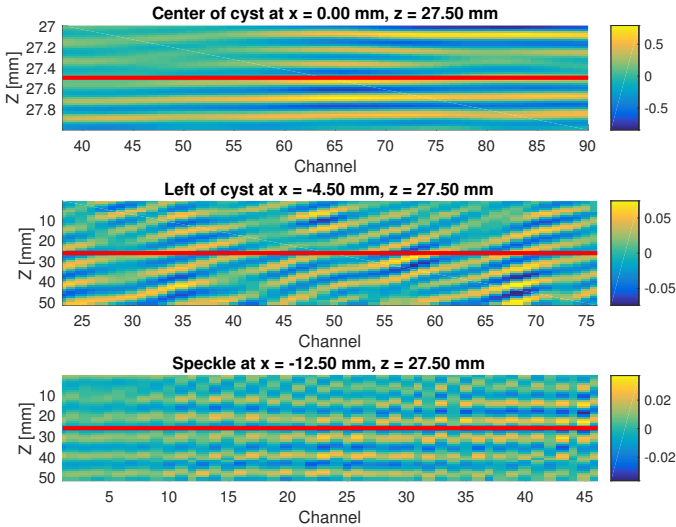

Fig. 6. The delayed wave-field for three different pixels in Fig. 1. The top is for the pixel at $x = 0.0$ mm and $z = 27.5$ mm inside the hyperechoic cyst, the middle is for the pixel at $x = -4.5$ mm and $z = 27.5$ mm to the left of the hyperechoic cyst, and the lower plot is for the pixel in speckle at $x = -12.5$ mm and $z = 27.5$ mm. The red line in the plot indicates the signals contributing in the sum of "delay-and-sum" beamforming when estimating the amplitude in the pixel.

The EBMV method does not use the *coherence* over the aperture directly. Instead, it estimates the spatial coherence matrix, and divides it into a signal space depending on the eigenstructure of the matrix. However, when we have a delayed wave-field with wave-fronts that are not parallel to the receiving aperture, the signal space estimated might not contain the steering vector $\mathbf{a} = 1$ entirely. Therefore, the projected weights will not fulfill the distortionless response constraint completely, with the consequence of a reduced output amplitude, resulting in the DRA.

Fig. 2 and 4 show the estimated CR for the simulated and the experimental images, respectively. We can clearly observe that the choice of background region for the CR calculation highly influences the estimated CR. Background region 2 and 3 are in both the simulated and experimental case influenced by the DRA and thus the estimated CR is artificially higher compared to background region 4, which was chosen to minimize the effect of the DRA. The methods not effected by the DRA, DAS and MV, have approximately the same CR for all three background regions. We can also observe that there is a large difference in the CR between the methods, especially the methods affected by the DRA have much higher CR when using background regions containing the DRA. However, we can also observe that the CF, GCF, PCF and DMAS, the beamformers using the coherence over the aperture in the beamforming, have a higher CR even when using background region 4 not affected by the DRA. It is worth to point out that the hyperechoic cyst was simulated to be 30 dB stronger than the background, and thus the CR should be 30 dB for the simulated case. This is true for DAS and MV for all background regions, and for EBMV when using the background region not affected by the DRA. The reason CF, GCF, PCF and DMAS results in images with CR higher than 30 dB could be because they stretch the dynamic range [1].

When comparing the simulated dataset in Fig. 1 and the experimental data in Fig. 3 we can observe that the DRA is much more visible in the simulated dataset. From Fig. 2 and 4 we see that the CR of the hyperechoic cyst for DAS in the simulated dataset is 30 dB stronger than the background speckle, while for the experimental it is only approximately 15 dB stronger. This indicates that the DRA only appears when a region is sufficiently strong compared to the background. This statement is confirmed by the point scatterer in Fig. 3. This point scatter is 35 dB stronger than the background speckle, and therefore the DRA is more distinct. Also, in Fig. 1 it was simulated a point scatterer at $x = 7.5$ mm and $z = 20$ mm that was only 10 dB stronger than the background speckle. From the images we can observe that this was not strong enough to produce the DRA.

VI. CONCLUSIONS

This study has investigated the dark region artifact (DRA) created by some adaptive beamformers. The DRA is observed next to targets that are sufficiently stronger than the surrounding background speckle. The measured CR can be invalid for the beamformers affected by the DRA if the background region is not carefully selected. The DAS and MV beamformers are not affected by the DRA, while CF, GCF, PCF and DMAS are affected because the delayed wave-field have wave-fronts that are not parallel to the receiving aperture and therefore creates low coherence. For the EBMV beamforming method the DRA is created because the steering vector is not completely contained in the signal space, resulting in a weightset reducing the output amplitude.

REFERENCES

[1] O. M. H. Rindal, A. Austeng, H. Torp, S. Holm, and A. Rodriguez-Molares, "The dynamic range of adaptive beamformers," *IEEE International Ultrasonics Symposium, IUS*, no. 1, pp. 1–4, 2016.

[2] J.-F. Synnevåg, A. Austeng, and S. Holm, "Benefits of minimum-variance beamforming in medical ultrasound imaging," *Ultrasonics, Ferroelectrics and Frequency Control, IEEE Transactions on*, vol. 56, no. 9, pp. 1868–1879, 2009.

[3] R. Mallart and M. Fink, "Adaptive focusing in scattering media through sound-speed inhomogeneities: The van Cittert Zernike approach and focusing criterion," *The Journal of the Acoustical Society of America*, vol. 96, no. 6, p. 3721, 1994.

[4] P. C. Li and M. L. Li, "Adaptive imaging using the generalized coherence factor," *IEEE Transactions on Ultrasonics, Ferroelectrics, and Frequency Control*, vol. 50, no. 2, pp. 128–141, 2003.

[5] J. Camacho, M. Parrilla, and C. Fritsch, "Phase coherence imaging," *IEEE Transactions on Ultrasonics, Ferroelectrics, and Frequency Control*, vol. 56, no. 5, pp. 958–974, 2009.

[6] G. Matrone, A. S. Savoia, G. Caliano, S. Member, and G. Magenes, "The Delay Multiply and Sum Beamforming Algorithm in Ultrasound B - Mode Medical Imaging," *IEEE Trans. Med. Imaging*, vol. 34, no. 4, pp. 1–10, 2015.

[7] B. M. Asl and A. Mahloojifar, "Eigenspace-based minimum variance beamforming applied to medical ultrasound imaging," *IEEE Transactions on Ultrasonics, Ferroelectrics, and Frequency Control*, vol. 57, no. 11, pp. 2381–2390, 2010.

[8] A. Rodriguez-Molares, O. M. H. Rindal, O. Bernard, A. Nair, M. A. Lediju Bell, H. Liebgott, A. Austeng, and L. Løvstakken, "The Ultra-Sound ToolBox (USTB)," *IEEE International Ultrasonics Symposium, IUS*, 2017.